

Article

Crystal Structure and Theoretical Investigation of Thiobarbituric Acid Derivatives as Nonlinear Optical (NLO) Materials

Anamika Sharma ^{1,2}, Assem Barakat ^{3,4}, Hessa H. Al-Rasheed ³,
Abdullah Mohammed Al-Majid ³, Sammer Yousuf ⁵, M. Iqbal Choudhary ^{5,6},
Ayman El-Faham ^{3,4,*}, Beatriz G. de la Torre ^{1,2} and Fernando Albericio ^{2,3,7,*}

¹ KwaZulu-Natal Research Innovation and Sequencing Platform (KRISP), School of Laboratory Medicine and Medical Sciences, College of Health Sciences, University of KwaZulu-Natal, Durban 4041, South Africa; anamika.aug14@gmail.com (A.S.); garciadelatorre@ukzn.ac.za (B.G.d.l.T.)

² Peptide Science Laboratory, School of Chemistry and Physics, University of KwaZulu-Natal, Westville, Durban 4000, South Africa

³ Department of Chemistry, College of Science, King Saud University, P.O. Box 2455, Riyadh 11451, Saudi Arabia; ambarakat@ksu.edu.sa (A.B.); halbahli@ksu.edu.sa (H.H.A.-R.); amajid@ksu.edu.sa (A.M.A.-M.)

⁴ Department of Chemistry, Faculty of Science, Alexandria University, P.O. Box 426, Ibrahimia, Alexandria 21321, Egypt

⁵ H.E.J. Research Institute of Chemistry, International Center for Chemical and Biological Sciences, University of Karachi, Karachi 75270, Pakistan; dr.sammer.yousuf@gmail.com (S.Y.); iqbal.choudhary@iccs.edu (M.I.C.)

⁶ Dr. Panjwani Center for Molecular Medicine and Drug Research, International Center for Chemical and Biological Sciences, University of Karachi, Karachi 75270, Pakistan

⁷ CIBER-BBN, Networking Centre on Bioengineering, Biomaterials and Nanomedicine, and Department of Organic Chemistry, University of Barcelona, Martí i Franqueés 1–11, 08028 Barcelona, Spain

* Correspondence: aelfaham@ksu.edu.sa (A.E.-F.); albericio@ukzn.ac.za (F.A.)

Received: 7 April 2020; Accepted: 9 May 2020; Published: 30 May 2020



Abstract: Here we report on the crystal structure of three enamine/imine TBA derivatives (1–3). Since the derivatives can take the form of enamine or imine tautomers, theoretical calculations were made to confirm that the former predominates due to higher stability (thermodynamic calculations). The enamines' form was further corroborated by high activation energy (ΔG^\ddagger ; which is >60 kcal/mol in all the cases), thus requiring a large amount of energy to pass the barrier (kinetics calculations). Furthermore, 1–3 were found to show high static hyperpolarizability (β_{tot}), thereby making them potential candidates as nonlinear materials for electro-optical devices and crystal engineering.

Keywords: crystals; Enamine/imine tautomer; DFT; NLO; hyperpolarizability

1. Introduction

Proper designing, or the development of new materials, requires accurate knowledge of molecular structure, which is accomplished by X-ray diffraction techniques [1–4]. Due to the interrelation of structure and application, accurate configuration plays a critical role [5]. Barbituric acid (BA) and thiobarbituric acid (TBA) derivatives have been known since the last century as pharmaceuticals [6]. These derivatives serve as antianxiety agents in the central nervous system by binding to the γ -aminobutyric acid (GABA) receptor. However, their potential as electro-optical materials has also been explored in crystal engineering [7–9]. Nonlinear optical (NLO) materials have found application

in optical storage communications and optical computing systems [8,10]. The budding field of NLO research and application requires extensive exploration of new materials for a large variety of processes [11]. Organically based NLO materials offer several advantages over inorganic systems, including high electronic susceptibility, high molecular polarizability and fast response time [12]. Although noncentrosymmetric crystals have found application as NLO materials, there are also a few reports where centrosymmetric crystals have been shown to possess NLO properties [12–15]. In recent years, BA/TBA-based derivatives have also been studied as NLO materials as they hold both hydrogen bond donors and acceptors, a feature that makes them suitable as crystal engineering materials with specific programmed properties [7,12,16–20].

Our group has synthesized BA/TBA-based derivatives for application in chemical biology [21–23]. Here we report on the crystal structures of three enamine/imine TBA derivatives (Figure 1) and provide confirmation of the tautomers by theoretical calculations. We also evaluate the hyperpolarizability of these compounds and thus their potential use as NLO materials.

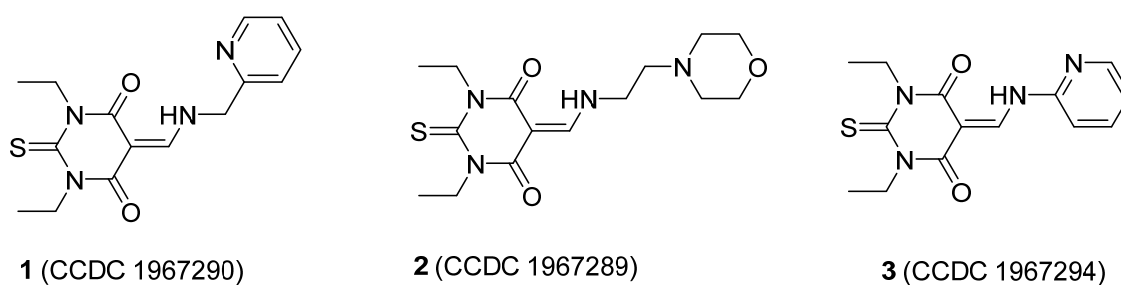


Figure 1. Structures of the three enamine/imine TBA derivatives 1–3.

2. Materials and Methods

2.1. General

Compounds 1–3 were synthesized as reported by our group earlier [23]. Melting points and ^1H NMR were in good agreement with the reported data. The X-ray crystallographic analysis was collected by using a Bruker SMART APEX II D8 Venture diffractometer (Karlsruhe, Germany) Gaussian09 (Wallingford, CT, USA) was used for theoretical calculations.

2.2. Structure Determination

The title compounds were obtained as crystalline materials obtained by recrystallization from ethanol with slow evaporation at room temperature. Data were collected on a Bruker APEX-II D8 Venture area diffractometer, equipped with graphite monochromatic Mo K $_{\alpha}$ radiation, $\lambda = 0.71073 \text{ \AA}$ at 100 (2) K. Cell refinement and data reduction were carried out using the Bruker SAINT program [24]. SHELXS was used to solve structure [25]. The final refinement was carried out using full matrix least squares techniques with anisotropic thermal data for nonhydrogen atoms. All the C-bound H atoms were located with idealized geometry and refined with C–H = 0.95–1.00 \AA having Uiso(H) = 1.5Ueq (CH $_3$) and 1.2Ueq (CH $_2$, CH, Aromatic-H). The N-bound H atoms were found in difference Fourier maps and their positions were freely refined with Uiso (H) = 1.2Ueq (N). CCDC 1967289, 1967290 and 1967294 contain the supplementary crystallographic data for these compounds and can be obtained free of charge from the Cambridge Crystallographic Data Centre via www.ccdc.cam.ac.uk/data_request/cif.

2.3. Theoretical Calculations

Based on the above crystal structures, a crystal unit was selected as the initial structure in each case. DFT-B3LYP/6–311G++(d,p) methods in Gaussian 09 [26] were used to optimize the structure of the title compounds. Vibration analysis showed that the optimized structure represented a minimum on the potential energy surface (no negative eigenvalues). TS calculations were performed using

the B3LYP functional and 6-311++G(d,p) basis set, and were confirmed by IRC calculations [27]. Static hyperpolarizability calculations were performed using the “polar” keyword in gaseous state and using the SCRF model. Methanol, chloroform and acetonitrile were used as solvents.

3. Results

All the derivatives (Figure 1) were synthesized earlier by our group and were well characterized by NMR and MS techniques [23].

3.1. Single Crystal X-ray Analysis

The single-crystal X-ray diffraction data of 1–3 were carried out by mounting suitable crystals for data collection. Data were collected on a Bruker D8 Venture equipped with a CCD Photon II detector and graphite monochromator with Cu K α radiation ($\lambda = 1.54178 \text{ \AA}$) at $T = 100 \text{ K}$. Data were integrated and reduced using the SAINT program [24]. Direct method and Fourier transformation techniques were used to solve the structures which were further refined by full matrix least squares techniques on F^2 using the SHELXL–2018 program (Table 1). Final refinement of the solved structures was carried out by means of the PLATON [28] and SHELXL programs [25]. The 3D structures were represented by an ORTEP diagram, while intermolecular interactions in the crystal packing were demonstrated by the Mercury program (Figure 2).

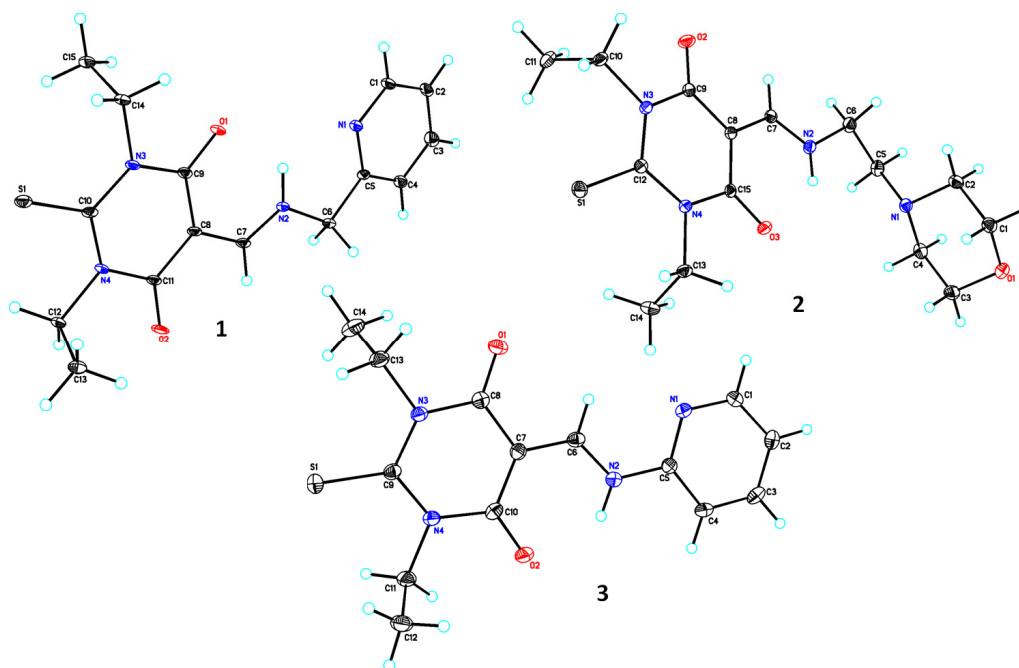


Figure 2. The ORTEP view of compounds 1–3 drawn at 30% probability level.

The structure of 1 was found to be similar to that of 3 with the difference being that, in the former, a pyridine ring (N1/C1–C5) was linked to 1,3-diethyl-2-thiobarbituric acid moiety (C7–C14/S1/N3–N4/O1–O2) via imine group (N2/C6) at C5 atom instead of *N*-methylmethanimine linkage. The dihedral angle between the pyridine ring (N1/C1–C5) and 1,3-diethyl-2-thiobarbituric acid moiety (C8–C15/S1/N3–N4/O1–O2) was $6.83(8)^\circ$, with a maximum deviation of $0.060(1) \text{ \AA}$ for N3 atom at r.m.s. plane.

Table 1. Summary of data collection and structure refinements of crystals 1–3.

#	1	2	3
Empirical formula	C ₁₅ H ₁₈ N ₄ O ₂ S	C ₁₅ H ₂₄ N ₄ O ₃ S	C ₁₄ H ₁₆ N ₄ O ₂ S
Formula weight	318.39	340.44	304.37
Temperature	100(2) K	100(2) K	173(2) K
Wavelength	1.54178 Å	1.54178 Å	1.54178 Å
Crystal system	Triclinic	Monoclinic	Monoclinic
Space group	P – 1	P 21/c	P 21/n
Unit cell dimensions	a = 4.8848(2) Å	a = 9.7627(3) Å	a = 11.3925(3) Å
	α = 93.6450(10)°	α = 90°	α = 90°
	b = 11.8126(4) Å	b = 19.5503(5) Å	b = 8.9642(3) Å
	β = 100.1890(10)°	β = 94.6850(10)°	β = 108.7440(10)°
	c = 13.2589(4) Å	c = 8.9301(3) Å	c = 14.6437(3) Å
	γ = 93.9350(10)°	γ = 90°	γ = 90°
Volume	748.99(5) Å ³	1698.74(9) Å ³	1416.17(7) Å ³
Z	2	4	4
Density (calculated)	1.412 Mg/m ³	1.327 Mg/m ³	1.428 Mg/m ³
Absorption coefficient	2.037 mm ⁻¹	1.839 mm ⁻¹	2.129 mm ⁻¹
F(000)	336	728	640
Crystal size (mm ³)	0.170 × 0.040 × 0.020	0.170 × 0.120 × 0.070	0.160 × 0.140 × 0.090
Theta range for data collection	3.397 to 68.333°.	4.523 to 68.224°.	5.877 to 68.226°.
Index ranges	−5 ≤ h ≤ 5	−11 ≤ h ≤ 11	−13 ≤ h ≤ 13
	−14 ≤ k ≤ 14	−23 ≤ k ≤ 23	−10 ≤ k ≤ 10
	−15 ≤ l ≤ 15	−10 ≤ l ≤ 10	−17 ≤ l ≤ 17
Reflections collected	19056	22428	40991
Independent reflections	2729 [R(int) = 0.0636]	3114 [R(int) = 0.0316]	2593 [R(int) = 0.0381]
Completeness to theta = 67.679°	100.0%	99.9%	99.6%
Refinement method	Full-matrix least-squares on F2	Full-matrix least-squares on F2	Full-matrix least-squares on F2
Data/restraints/parameters	2729/0/203	3114/0/212	2593/0/196
Goodness-of-fit on F2	1.067	1.054	1.089
Final R indices [I > 2sigma(I)]	R1 = 0.0598, wR2 = 0.1802	R1 = 0.0323, wR2 = 0.0846	R1 = 0.0353, wR2 = 0.0881
R indices (all data)	R1 = 0.0652, wR2 = 0.1868	R1 = 0.0347, wR2 = 0.0866	R1 = 0.0359, wR2 = 0.0885
Largest diff. peak and hole	0.622 and −0.672 e.Å ⁻³	0.737 and −0.240 e.Å ⁻³	0.396 and −0.241 e.Å ⁻³

The structure of **2** comprised a morpholine ring (C1-C4/O1/N1) in chair conformation linked to 1,3-diethyl-2-thiobarbituric acid moiety (C8-C15/S1/N3-N4/O2-O3) via an *N*-ethylmethanimine chain (C5-C6/N2) at the N1 atom. The dihedral angle between the morpholine ring (C1-C4/O1/N1) and 1,3-diethyl-2-thiobarbituric acid moiety (C8-C15/S1/N3-N4/O2-O3) was 89.96(7)°, with a maximum deviation of 0.245(1) Å for the O1 atom at r.m.s. plane.

The structure of **3** was formed by a pyridine ring (N1/C1-C5) linked to 1,3-diethyl-2-thiobarbituric acid moiety (C8-C15/S1/N3-N4/O1-O2) via an *N*-methylmethanimine chain (C6-C7/N2) at the C5 atom. The dihedral angle between the pyridine ring (N1/C1-C5) and 1,3-diethyl-2-thiobarbituric acid moiety (C8-C15/S1/N3-N4/O1-O2) was $3.48(10)^\circ$, with a maximum deviation of $0.025(2)$ Å for the N4 atom at r.m.s. plane.

3.2. Crystal Packing

In the crystal lattice of **1**, molecules interact with each other in parallel chains via H7A...O2 with a donor–acceptor distance of $3.174(3)$ Å to form the $R^2_2(10)$ ring motif. The $\pi\cdots\pi$, C–O... π and C–H... π interactions further strengthen the crystal structure with a Cg1–Cg1 (N1/C1-C5) distance of $4.8848(14)$ Å, Cg1–Cg2 (N1/C1-C5 and N3/N4/C8-C11) distance of $5.0633(13)$ Å, Cg2–Cg2 (N3/N4/C8-C11) distance of $4.8847(12)$ Å, O1...Cg2 (N3/N4/C8-C11) distance of $3.6957(17)$ Å and H12B...Cg2 (N3/N4/C8-C11) distance of 2.99 Å, respectively (Table 2, Figure 3).

Table 2. The list of selected hydrogen bonds' geometry Å in compound **1**.

D	H	A	D–H	H...A	D...A	D–H...A
C1	H25	O2	0.99	2.58	3.4464(18)	146
C5	H6	O1	0.95	2.60	3.4395(17)	148
C9	H9	O2	0.98	2.57	3.3370(18)	135
C15	H20	O3	0.99	2.40	3.3831(19)	171

Symmetric codes: $-X, 1/2 + Y, 1/2 - Z$.

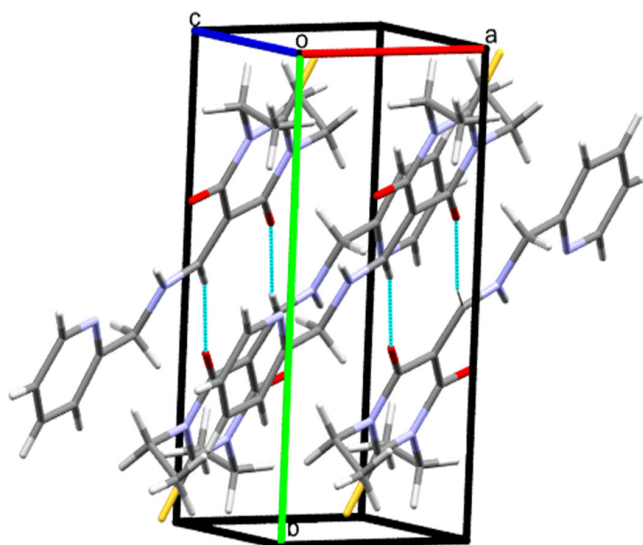


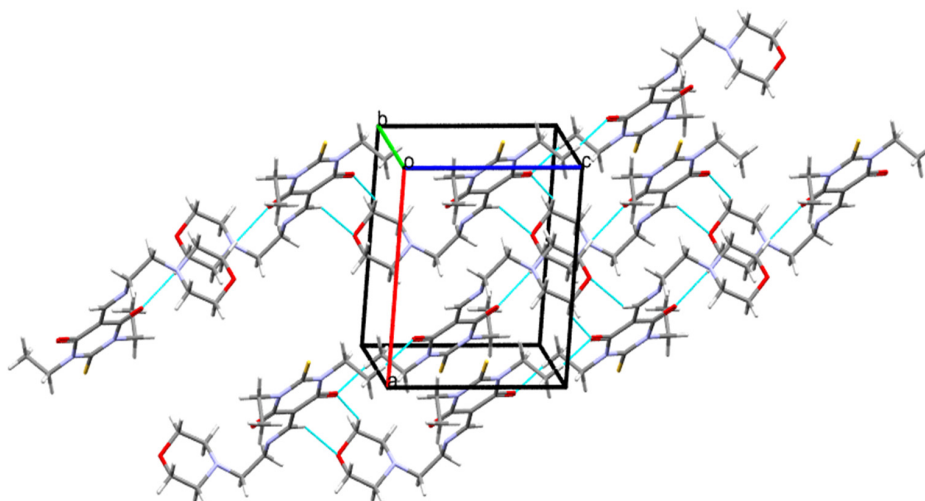
Figure 3. Crystal packing diagram of compound **1**.

In the crystal lattice of **2**, molecules are found to be connected in zigzag chains via H6...O1, H9...O2, H20...O3, H25...O2 with a donor–acceptor distance of $3.4395(17)$ Å, $3.3370(18)$ Å, $3.3831(19)$ Å and $3.4464(18)$ Å, respectively, to form a $R^2_2(8)$ ring motif. The $\pi\cdots\pi$ and C–H... π interactions further strengthen the crystal structure with a Cg2–Cg2 (N3–N4/C6–C7/C10/C13) distance of $3.4573(7)$ Å and H19...Cg2 (N3–N4/C6–C7/C10/C13) distance of 2.91 Å, respectively (Table 3, Figure 4).

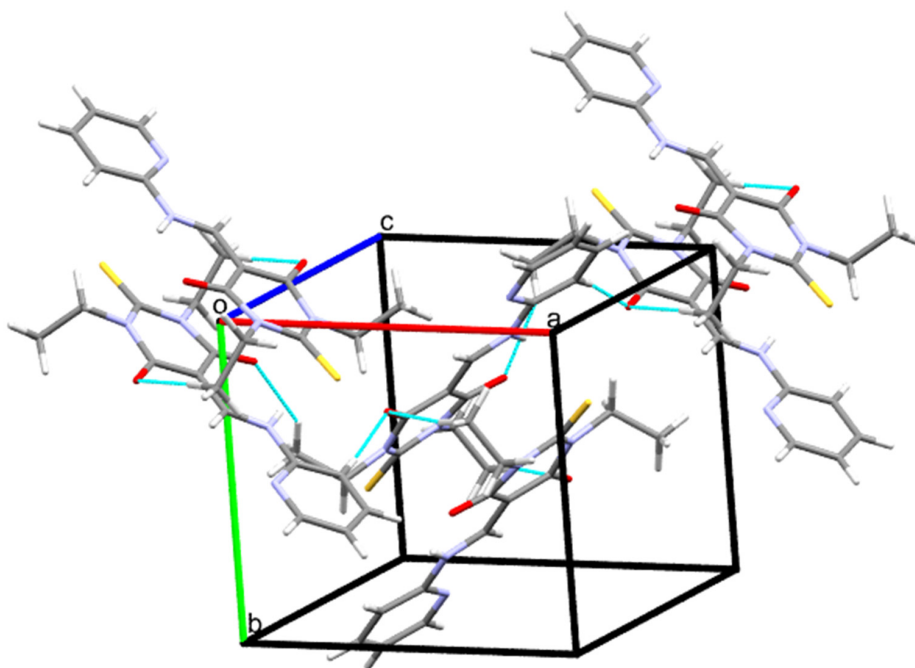
In the crystal lattice of **3**, molecules are linked via H4...O1, H12A...O1, and H14C...O2 with a donor–acceptor distance of $3.3420(19)$ Å, $3.531(2)$ Å and $3.442(2)$ Å, respectively. The $\pi\cdots\pi$, C–O... π and C–S... π interactions further strengthen the crystal structure with a Cg1–Cg1 (N1/C1-C5) distance of $5.6787(10)$ Å, Cg1–Cg2 (N1/C1-C5 and N3/N4/C7-C10) distance of $3.6959(9)$ Å, Cg2–Cg2 (N3/N4/C7-C10) distance of $3.9269(9)$ Å, O1...Cg1 (N1/C1-C5) distance of $3.9718(14)$ Å and S1...Cg1 (N1/C1-C5) distance of $3.7580(8)$ Å (Table 4, Figure 5).

Table 3. The list of selected hydrogen bond Å in compound 2.

D.	H	A	D-H	H...A	D...A	D-H...A
C7	H7A	O2	0.95	2.28	3.174(3)	156

Symmetric codes: $-x, -y, -z$.**Figure 4.** Crystal packing diagram of compound 2.**Table 4.** The list of selected hydrogen bond Å in compound 3.

D	H	A	D-H	H...A	D...A	D-H...A
C4	H4	O1	0.95	2.40	3.3420(19)	172
C12	H12A	O1	0.98	2.58	3.531(2)	163
C14	H14C	O2	0.98	2.58	3.442(2)	147

Symmetric codes: $-x + 1/2, y + 1/2, -z + 1/2$.**Figure 5.** Crystal packing diagram of compound 3.

3.3. Hirshfeld Surface Analysis

Figure 6 shows the Hirshfeld surface mapped over d_{norm} based on van der Waals radii of all three crystals. Dark blue indicates positive d_{norm} values (contacts longer than the van der Waals radii), dark red indicates negative d_{norm} values (contacts shorter than the sum of van der Waals radii) and white indicates zero values d_{norm} (contact distances close to van der Waals). Figure 7 shows the percentage contribution of each bond in the molecule. The central sharp spike of the fingerprint plot corresponds to the H–H-type intermolecular interactions for 1–3, which was found to be 51.7%, 62.7% and 52.9% respectively. The O–H/H–O interactions in 1–3 (11.5%, 17.1% and 11.8% respectively) are shown by the large spikes on both sides. The percentage of contribution of C–H-type interactions in the total Hirshfeld surface in 1–3 in the total Hirshfeld surface is 15.6%, 5.9% and 6.6% respectively. Figure 7 shows the interhydrogen bonding pattern in the three crystals. The bond distances were found to be in good agreement with those of crystal data. Figure 8 shows the electronic cloud around the molecule along with interactions with the adjacent molecule. The red circles in each structure indicate areas of high hydrogen bonding, whereas the white circles indicate the weak van der Waals force of attraction.

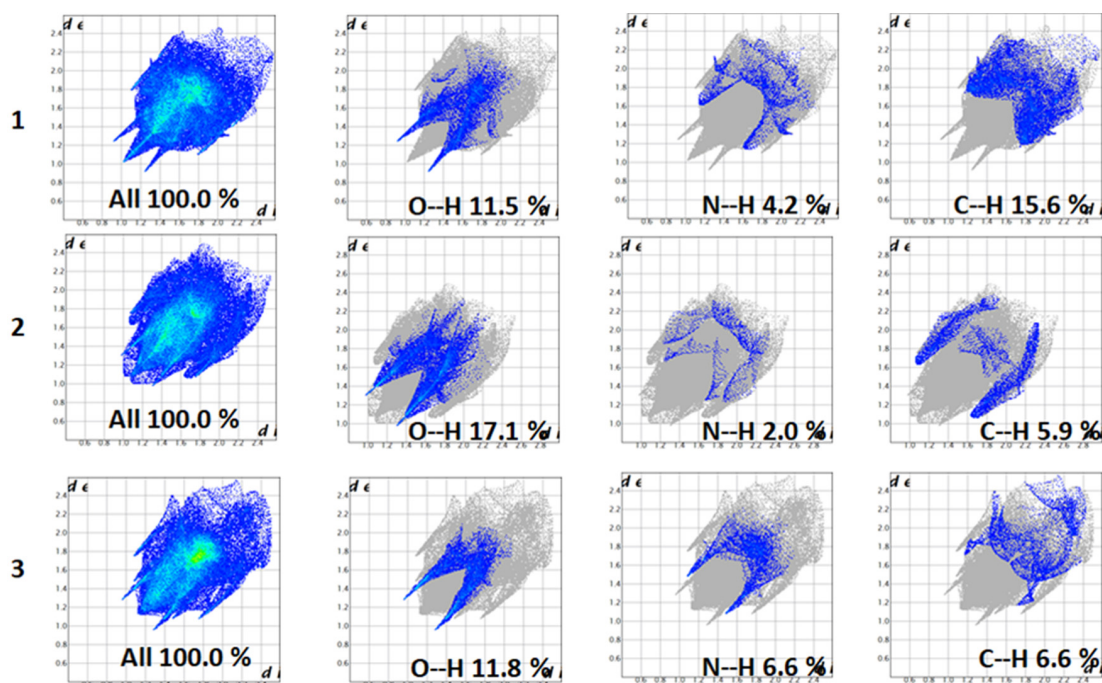


Figure 6. Fingerprint plot for compounds 1–3 showing percentages for all interactions and O–H, N–H and C–H contacts in the total Hirshfeld surface area.



Figure 7. Percentage contribution of each interaction between atoms in 1–3.

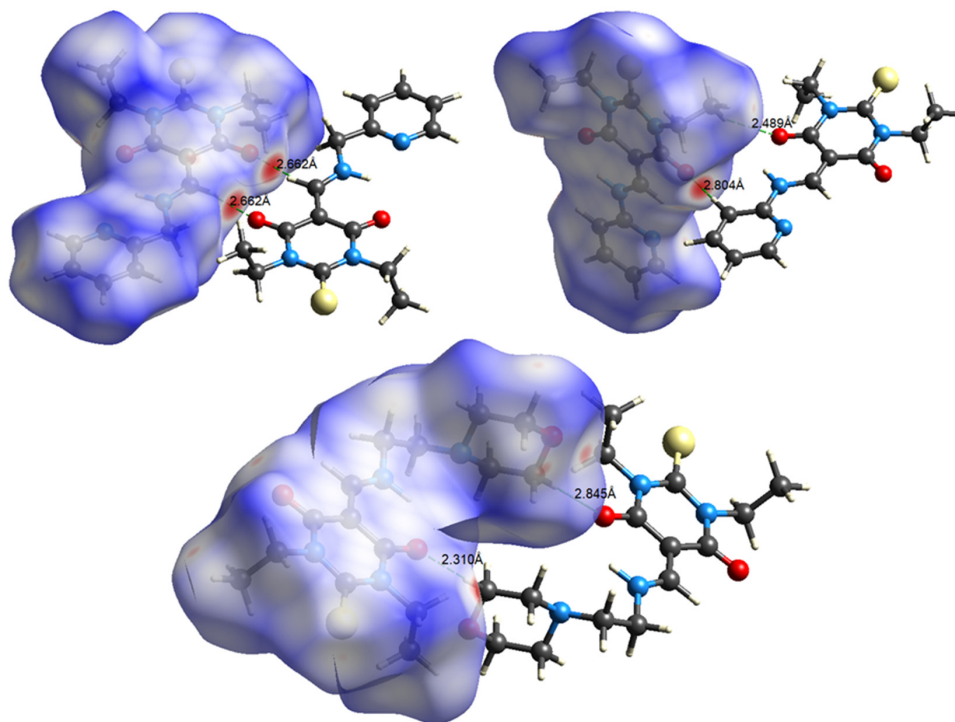


Figure 8. Hirshfeld surfaces mapped with d_{norm} shape-index and curvedness properties along with molecular pairs involving hydrogen bond interactions.

3.4. Theoretical Calculations

Density functional theory (DFT) calculations were performed in the gaseous phase with the Gaussian 09 program, using the B3LYP correlation function and 6-311G++(d,p) basis set [26]. Geometry optimization was performed in the gaseous phase. No solvent corrections were made with these calculations as gaseous phase calculations frequently correspond well with crystal structures. Starting geometries were taken from X-ray refined data. The optimized geometry results in the free molecule state were compared to those in the crystalline state (Figure 9). No negative vibrational modes were obtained. The DFT calculated structure and geometric parameters (bond lengths and bond angles) were compared to those of X-ray data and were found to be consistent with the experimental data.

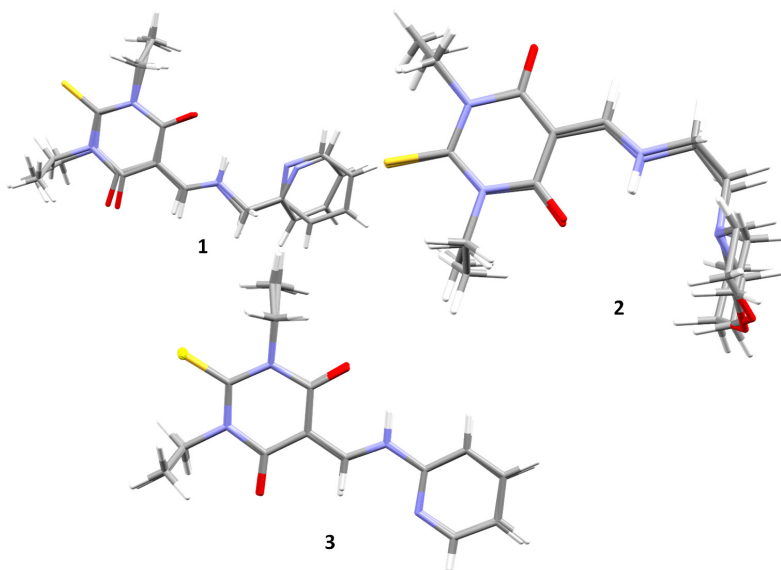


Figure 9. Overlay of crystal structures and optimized geometry of 1–3.

Frontier molecular orbitals (FMO) in all three cases were analyzed. The electron density in the HOMO for all cases was high over the thiobarbituric ring. However, electron density in LUMO was localized mainly on the pyridine ring in the case of **1** and **3**. In **2**, the density was localized throughout the thiobarbituric ring (Figure 10).

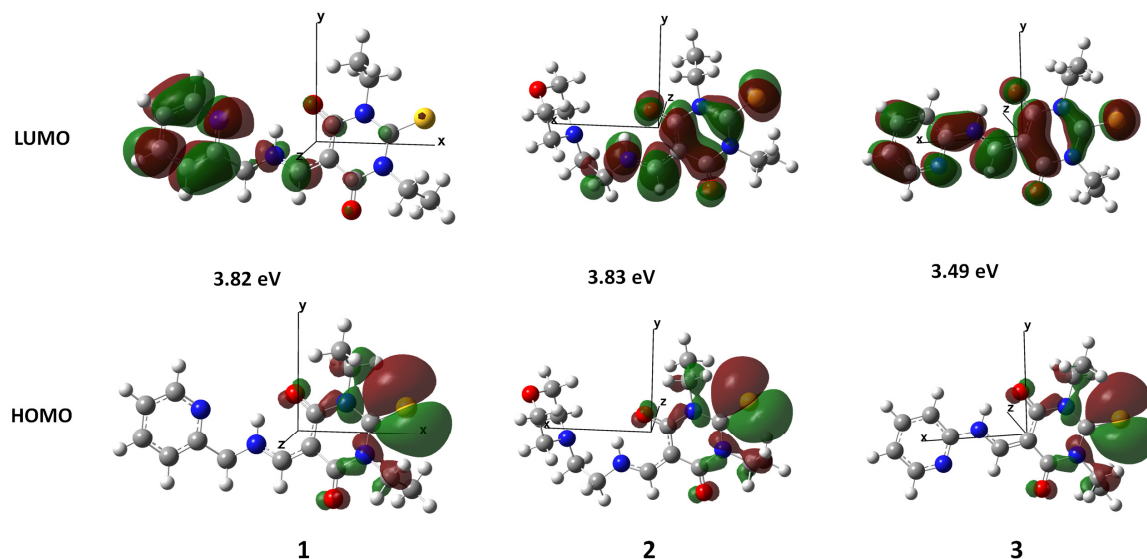


Figure 10. HOMO and LUMO molecular orbitals in 1–3 with band gap in each case.

The HOMO–LUMO gap (which helps to predict the reactivity of the compound) was calculated for the three molecules (Table 5). The HOMO–LUMO gap in **3** (3.49 eV) was smaller than **1** (3.82 eV) and **2** (3.83 eV), thereby indicating its high reactivity [29].

Table 5. Total energy and frontier orbital energy.

	1	2	3
E_{total} in Hartree	−1350.42096974	−1429.26867147	−1311.10670189
E_{HOMO} in Hartree	−0.21654	−0.21799	−0.22352
E_{LUMO} in Hartree	−0.07593	−0.07714	−0.09533
ΔE^* in Hartree (eV)	0.14061 (3.82)	0.14085 (3.83)	0.12819 (3.49)

* $\Delta E = \text{LUMO-HOMO}$; 1 Hartree = 27.2 eV

3.5. Transition State Calculations

A transition state (TS) is a first-order saddle point on the potential energy surface (PES) of the molecular system and it is characterized by one imaginary frequency (implying a negative force constant). One imaginary frequency implies that the energy has a maximum energy in one direction in nuclear configurational space, while in all other orthogonal directions the energy is a minimum [30].

The title compound(s) can exist in tautomeric form as shown in Figure 11. The crystal structures confirm that the molecules exist as **I** form.

To confirm the form, DFT calculations were made using the B3LYP functional and 6-311++G(d,p) basis set. All the thermodynamic parameters (ΔH° , ΔS° , and $\Delta G^{\circ\#}$) were calculated at default temperature (298.15 K) and pressure (1 atm). The TS in all cases was confirmed by intrinsic reaction coordinate (IRC) calculations. Activation energy was calculated in all cases, as shown in Table 6 and schematically in Figure 12. The thermodynamic calculations reveal that form **I** was more predominant as compared to **II** in all cases, as indicated by large positive values of ΔH° and ΔG° . This finding was further confirmed by calculation of the TS in all cases. Figure 11 shows the higher stability of **I** (low energy) as compared to **II** (high energy). This observation also confirms that when a product is present

in **I** form, it will not convert to **II** at room temperature as it would require high energy to pass the large activation energy barrier (ΔG^\ddagger).

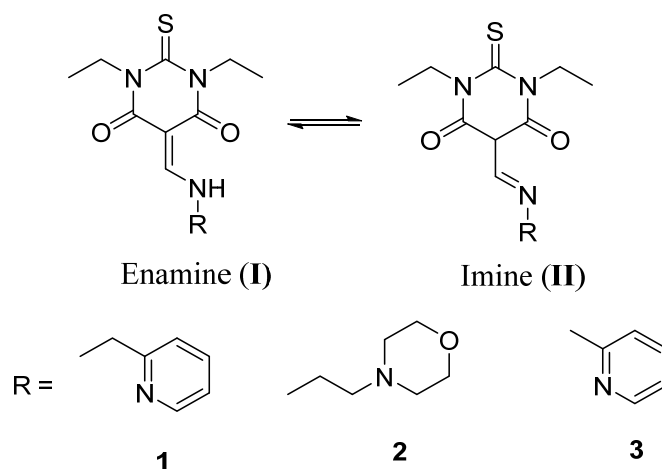


Figure 11. Enamine/imine tautomeric forms of compounds 1–3.

Table 6. Calculated reaction profile using the 6–31G++(d,p) basis set.

Properties	Compound	ΔH° (kcal/mol)	$\Delta G^{\circ\ddagger}$ (kcal/mol/K)	ΔS° (cal/mol)
Thermodynamics	1	24.2	23.4	3.0
	2	27.2	26.5	2.5
	3	26.8	25.5	4.5
Kinetics	1	60.8	60.5	1.1
	2	61.8	61.1	2.3
	3	64.3	63.7	2.1

#In case of Kinetics, ΔG° refers to activation energy ($\Delta G^{\circ\ddagger}$)

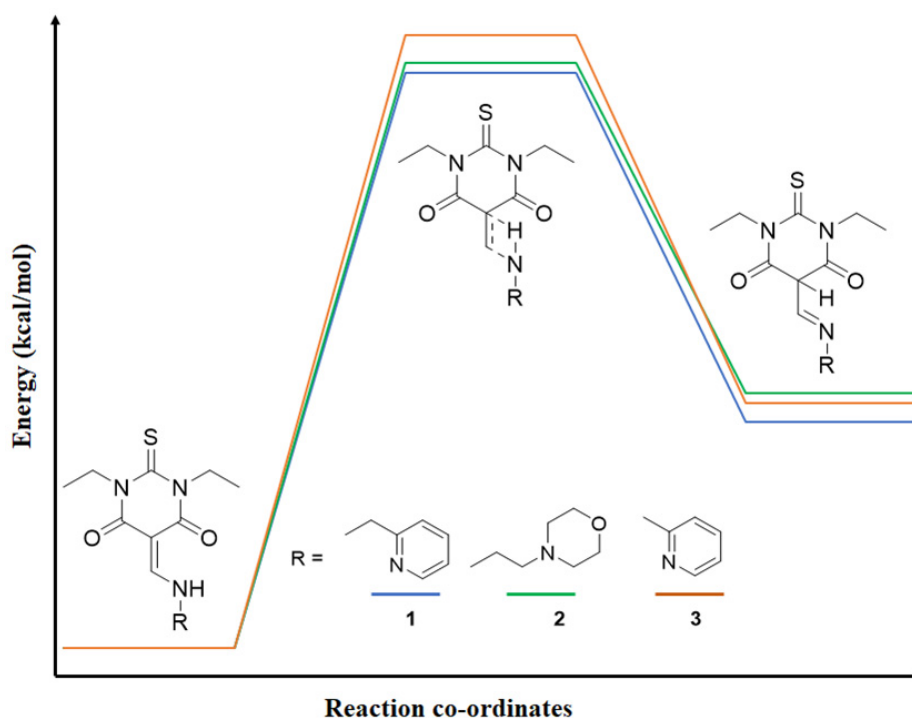


Figure 12. Transition state for intramolecular conversion for all compounds 1–3.

3.6. NLO Calculations

The design of new NLO materials is dependent mainly on the synthesis of chromophores with large first or higher-order hyperpolarizabilities. The calculations of the dipole moment, linear and static first-order hyperpolarizability were performed using the 6-311G++(d,p) basis set and the following equations: employing Kleinmann symmetry, the third-rank tensor for hyperpolarizability has been described by 3D matrix and hence reduced to 10 components. The dipole moment, linear polarizability and first-order hyperpolarizability of the three derivatives were calculated by taking the Cartesian coordinate system at the centre of mass of the compound by a finite field of approach, and the results are shown in Table 7.

$$\mu_0 = \sqrt{\mu_x^2 + \mu_y^2 + \mu_z^2}$$

$$\alpha_0 = \frac{1}{3}(\alpha_{xx} + \alpha_{yy} + \alpha_{zz})$$

$$\beta_0 = \sqrt{(\beta_{xxx} + \beta_{xyy} + \beta_{xzz})^2 + (\beta_{yyy} + \beta_{yzz} + \beta_{yxx})^2 + (\beta_{zzz} + \beta_{zxx} + \beta_{zyy})^2}$$

Table 7. Dipole moment, linear polarizability and static hyperpolarizability components in gaseous state.

Parameter	Gaseous			Chloroform			Methanol			Acetonitrile		
	1	2	3	1	2	3	1	2	3	1	2	3
μ_x	-7.40	5.22	5.78	-9.82	6.72	7.67	-11.29	7.34	8.43	-10.72	7.34	8.44
μ_y	-1.35	-2.70	1.92	-2.10	-3.81	2.55	-2.71	-4.42	2.88	-2.58	-4.42	2.88
μ_z	0.41	0.48	0.34	0.24	0.37	0.41	0.01	0.34	0.47	0.08	0.34	0.47
total (μ)	7.53	5.90	6.10	10.04	7.73	10.01	11.62	8.57	8.92	11.02	8.57	8.93
α_{xx}	-123.63	-163.28	-112.49	-119.27	-169.93	-109.52	-115.29	-173.27	-109.15	-118.15	-173.27	-109.15
α_{yy}	-138.94	-150.12	-132.80	-137.75	-150.10	-132.86	-136.70	-150.14	-133.00	-137.42	-150.14	-133.01
α_{zz}	-136.63	-142.71	-133.62	-137.91	-141.68	-133.67	-139.64	-141.15	-133.65	-138.18	-141.15	-133.65
α_{xy}	3.23	-10.22	5.78	4.12	-12.19	7.48	4.58	-12.84	8.35	4.93	-12.84	8.37
α_{xz}	-9.15	-1.02	1.15	-8.78	-1.89	1.34	-5.05	-1.92	1.45	-8.13	-1.92	1.46
α_{yz}	2.38	1.94	0.13	2.72	2.36	-0.04	2.18	2.44	-0.04	3.00	2.44	-0.04
α (esu) $\times 10^{-23}$	1.97	2.25	1.87	1.95	2.28	1.86	1.93	2.29	1.86	1.95	2.29	1.86
β_{xxx}	-237.81	21.77	282.13	-339.44	38.91	357.94	-416.28	47.41	388.35	-381.27	47.41	388.86
β_{yyy}	31.96	17.08	23.85	34.02	13.10	29.10	32.53	9.98	31.57	33.25	9.98	31.62
β_{zzz}	-5.15	-1.91	-0.88	-6.16	-0.53	-0.68	-5.15	-0.21	-0.54	-6.84	-0.21	-0.54
β_{xyy}	-26.81	44.25	-2.89	-43.30	52.91	-1.12	-59.00	57.40	-0.50	-48.58	57.40	-0.48
β_{xxy}	-38.97	-100.23	-5.76	-58.43	-127.04	-1.98	-73.38	-139.33	0.21	-69.70	-139.33	0.25
β_{xxz}	53.09	0.11	1.00	53.85	0.29	1.15	36.45	2.03	1.82	51.44	2.03	1.84
β_{xzz}	-11.70	34.96	-13.90	-5.64	41.18	-12.51	5.96	44.08	-11.84	-3.45	44.08	-11.83
β_{yzz}	-8.76	1.32	-0.53	-8.00	0.23	0.01	-5.88	-0.44	0.29	-7.60	-0.44	0.29
β_{yyz}	-1.97	1.47	4.43	-5.84	-0.31	5.05	-8.22	-0.64	5.38	-6.85	-0.64	5.39
β_{xyz}	-14.66	6.14	1.46	-12.94	6.02	0.86	-8.65	6.35	0.95	-13.71	6.35	0.95
β (esu) $\times 10^{-31}$	2.42	1.12	2.30	3.39	1.51	2.98	4.08	1.71	3.26	3.78	1.71	3.27

The calculation was initially performed in gaseous state. Furthermore, to analyze the effect of solvents, three solvents; namely, methanol, chloroform and acetonitrile, were chosen. Methanol and acetonitrile are polar protic and polar aprotic solvents respectively, whereas chloroform is nonpolar [11,31]. Dielectric constant plays a crucial role in determining NLO properties [11,32]. Although acetonitrile and methanol showed different behaviors, their dielectric constant was comparable (37.5 for acetonitrile and 33 for methanol). However, the dielectric constant of chloroform was only 4.8. According to the literature, the higher the dielectric constant, the better the NLO properties. Static hyperpolarizability (β_{tot}) in all cases was comparable for methanol and acetonitrile, which in turn were higher than that of chloroform (Table 8). The β_{tot} in all cases was higher than that of urea (0.3728×10^{-30} esu), which, as an NLO material [33], is considered a reference for comparison. Theoretical calculations also support the relevance of solvents in NLO properties, as these properties increased from gaseous to solvent (Table 8). Of the three derivatives, compounds 1 and 3 showed potential as NLO materials, due to their high μ_{tot} and β_{tot} and small band gap, as reflected by the frontier orbitals.

Table 8. Comparison of dipole moment (μ_{tot}) and static hyperpolarizability (β_{tot}) in three solvents.

	μ ($\times 10^{-30}$ esu) *			β ($\times 10^{-30}$ esu) *		
	1	2	3	1	2	3
Gaseous	7.53	5.90	6.10	2.96	1.38	2.40
Acetonitrile (ACN)	11.02	8.57	8.93	4.10	2.07	3.36
Chloroform (CHCl ₃)	10.04	7.73	10.01	3.76	1.84	3.09
Methanol (MeOH)	11.62	8.57	8.92	4.09	2.07	3.36

* $\beta = 6-311\text{G}++(\text{d,p})$.

4. Conclusions

In summary, we report here the crystal structures of three enamine/imine TBA derivatives (1–3). These derivatives are known to exist in several tautomeric forms. In the enamine and imine equilibrium, the former predominates due to high stability (as confirmed by thermodynamics calculations using DFT). The equilibrium is highly favourable towards enamine. This was further confirmed by TS calculations, as the activation energy is very high, thus requiring a large amount of energy to pass the barrier (ΔG^\ddagger ; which is >60 kcal/mol in all the cases). Due to their hydrogen bond donors and acceptor properties, NLO calculations were performed. Enamine/imine TBA derivatives (1–3) all showed high static hyperpolarizability (β_{tot}). The solvent effect on β_{tot} was also studied. It was found that the high dielectric constant of solvents contributes to the NLO properties of the derivatives, thereby making them potential candidates as nonlinear materials for electro-optical application in crystal engineering.

Supplementary Materials: The supplementary information is available online at <http://www.mdpi.com/2073-4352/10/6/442/s1>.

Author Contributions: The work was designed by A.S., A.B., A.E.-F., B.G.d.I.T., and F.A.; synthesis was carried out by H.H.A.-R. and A.M.A.-M. under the supervision of A.B., crystal structure was determined by S.Y. and M.I.C.; calculations were made by A.S. All authors contributed in the results and discussion. The first draft of the manuscript was prepared by A.S. and all authors were contributed in the final version. All authors have read and agreed to the published version of the manuscript.

Funding: The work in the author's laboratory was funded in part by the following: The Deanship of Scientific Research at King Saud University, for providing funding to the research group no. RG-1441-365, Saudi Arabia; National Research Foundation (NRF) and the University of KwaZulu-Natal (South Africa); the Spanish Ministry of Economy, Industry, and Competitiveness (MINECO) (RTI2018-093831-B-100), CIBER-BBN, and the Generalitat de Catalunya (2017 SGR 1439) (Spain).

Conflicts of Interest: The authors declare no conflict of interest.

References

1. Shell, J.W. X-ray and Crystallographic Applications in Pharmaceutical Research II. *J. Pharm. Sci.* **1963**, *52*, 24–29. [[CrossRef](#)] [[PubMed](#)]
2. Deschamps, J. The role of crystallography in drug design. *AAPS J.* **2005**, *7*, E813–E819. [[CrossRef](#)] [[PubMed](#)]
3. Aitipamula, S.; Vangala, V.R. X-Ray Crystallography and its Role in Understanding the Physicochemical Properties of Pharmaceutical Cocrystals. *J. Indian Inst. Sci.* **2017**, *97*, 227–243. [[CrossRef](#)]
4. Zheng, H.; Hou, J.; Zimmerman, M.; Wlodawer, A.; Minor, W. The future of crystallography in drug discovery. *Expert Opin. Drug Deliv.* **2013**, *9*, 125–137. [[CrossRef](#)]
5. Mason, S. Molecular structure and biological activity. *Trends Biochem. Sci.* **1983**, *8*, 422–423. [[CrossRef](#)]
6. Jursic, B.S.; Neumann, N.M.; Bowdy, K.L.; Stevens, E.D. Simple, efficient, high yield syntheses of substituted and unsubstituted 5-benzoylbarbituric acids, and their corresponding schiff base phenylhydrazones. *J. Heterocycl. Chem.* **2004**, *41*, 233–246. [[CrossRef](#)]
7. Kondo, K.; Fukutome, M.; Ohnishi, N.; Aso, H.; Kitaoka, Y.; Sasaki, T. Laser Properties of Nonlinear Optical Benzal Barbituric Acid Crystals. *Jpn. J. Appl. Phys.* **1991**, *30*, 3419–3420. [[CrossRef](#)]
8. Knill, E.; Laflamme, R.; Milburn, G.J. A scheme for efficient quantum computation with linear optics. *Nature* **2001**, *409*, 46–52. [[CrossRef](#)]

9. Feng, J.-D.; Yan, L.-K.; Su, Z.; Kan, Y.; Lan, Y.-Q.; Liao, Y.; Zhu, Y.-L. Theoretical Studies on Electronic Spectra and Second-order Nonlinear Optical Properties of Glucosyl Substituted Barbituric Acid Derivatives. *Chin. J. Chem.* **2006**, *24*, 119–123. [[CrossRef](#)]
10. Smith, S.D. Lasers, nonlinear optics and optical computers. *Nature* **1985**, *316*, 319–324. [[CrossRef](#)]
11. Cammi, R.; Mennucci, B.; Tomasi, J. Solvent Effects on Linear and Nonlinear Optical Properties of Donor–Acceptor Polyenes: Investigation of Electronic and Vibrational Components in Terms of Structure and Charge Distribution Changes. *J. Am. Chem. Soc.* **1998**, *120*, 8834–8847. [[CrossRef](#)]
12. Ivanova, B.B.; Spittler, M. Possible Application of the Organic Barbiturates as NLO Materials. *Cryst. Growth Des.* **2010**, *10*, 2470–2474. [[CrossRef](#)]
13. Amudha, M.; Rajkumar, R.; Thayanithi, V.; Kumar, P.P. Growth and Characterization of Benzimidazolium Salicylate: NLO Property from a Centrosymmetric Crystal. *Adv. Opt. Technol.* **2015**, *2015*, 1–9. [[CrossRef](#)]
14. Arulmozhi, S.; Madhavan, J. Molecular structure, First-order hyperpolarizability and HOMO-LUMO studies of L- Histidinium Dinitrate. *IOP Conf. Ser.: Mater. Sci. Eng.* **2015**, *73*, 012035. [[CrossRef](#)]
15. Nalla, V.; Medishetty, R.; Wang, Y.; Bai, Z.; Sun, H.; Wei, J.; Vittal, J.J. Second harmonic generation from the ‘centrosymmetric’ crystals. *IUCr* **2015**, *2*, 317–321. [[CrossRef](#)] [[PubMed](#)]
16. Cao, Y.-W.; Chai, X.-D.; Chen, S.-G.; Jiang, Y.-S.; Yang, W.-S.; Lu, R.; Ren, Y.-Z.; Blanchard-Desce, M.; Li, T.-J.; Lehn, J.-M. A new series of nonlinear optical organic materials with molecular receptor: Design and synthesis. *Synth. Met.* **1995**, *71*, 1733–1734. [[CrossRef](#)]
17. Gryl, M.; Kozieł, M.; Stadnicka, K.; Matulková, I.; Němec, I.; Mrkyvkova, N.; Němec, P. Lidocaine barbiturate: A promising material for second harmonic generation. *CrystEngComm* **2013**, *15*, 3275. [[CrossRef](#)]
18. Moylan, C.R.; Twieg, R.J.; Lee, V.Y.; Swanson, S.A.; Betterton, K.M.; Miller, R.D. Nonlinear optical chromophores with large hyperpolarizabilities and enhanced thermal stabilities. *J. Am. Chem. Soc.* **1993**, *115*, 12599–12600. [[CrossRef](#)]
19. Sun, G.; Qiu, Y.-Q.; Sun, H.-Z.; Su, Z.; Feng, J.-D.; Zhu, Y.-L. Theoretical studies on electronic spectra and second-order nonlinear optical properties of barbituric acid derivatives substituted with schiff base. *Chin. J. Chem.* **2010**, *22*, 425–429. [[CrossRef](#)]
20. Tron, A.; Rocher, M.; Thornton, P.J.; Tucker, J.H.R.; McClenaghan, N.D. Supramolecular Architectures Incorporating Hydrogen-Bonding Barbiturate Receptors. *Asian J. Org. Chem.* **2015**, *4*, 192–202. [[CrossRef](#)]
21. Sharma, A.; Noki, S.; Zamisa, S.J.; Hazzah, H.A.; Almarhoon, Z.; El-Faham, A.; De La Torre, B.G.; Albericio, F.; Noki, S. Exploiting the Thiobarbituric Acid Scaffold for Antibacterial Activity. *ChemMedChem* **2018**, *13*, 1923–1930. [[CrossRef](#)] [[PubMed](#)]
22. Sharma, A.; Zamisa, S.J.; Noki, S.; Almarhoon, Z.; El-Faham, A.; De La Torre, B.G.; Albericio, F. Crystal structure, spectroscopic studies and theoretical studies of thiobarbituric acid derivatives: Understanding the hydrogen-bonding patterns. *Acta Crystallogr. C Struct. Chem.* **2018**, *74*, 1703–1714. [[CrossRef](#)] [[PubMed](#)]
23. Ali, M.; Barakat, A.; El-Faham, A.; Al-Rasheed, H.H.; Dahlous, K.; Al-Majid, A.M.; Sharma, A.; Yousuf, S.; Sanam, M.; Ul-Haq, Z.; et al. Synthesis and characterisation of thiobarbituric acid enamine derivatives, and evaluation of their α -glucosidase inhibitory and anti-glycation activity. *J. Enzym. Inhib. Med. Chem.* **2020**, *35*, 692–701. [[CrossRef](#)] [[PubMed](#)]
24. Bruker, A. *SAINTE Software Reference Manual*; Bruker AXS, Inc.: Madison, WI, USA, 1998.
25. Sheldrick, G.M. Crystal structure refinement with SHELXL. *Acta Crystallogr. C* **2015**, *71*, 3–8. [[CrossRef](#)] [[PubMed](#)]
26. Frisch, M.J.; Trucks, G.; Schlegel, H.; Scuseria, G.; Robb, M.; Cheeseman, J.; Scalmani, G.; Barone, V.; Mennucci, B.; Petersson, G. *Gaussian 09, Revision D. 01*; Gaussian, Inc.: Wallingford, CT, USA, 2009.
27. Gonzalez, C.; Schlegel, H.B. Reaction path following in mass-weighted internal coordinates. *J. Phys. Chem.* **1990**, *94*, 5523–5527. [[CrossRef](#)]
28. Spek, A.L. Single-crystal structure validation with the program PLATON. *J. Appl. Crystallogr.* **2003**, *36*, 7–13. [[CrossRef](#)]
29. Aihara, J.-I. Correlation found between the HOMO–LUMO energy separation and the chemical reactivity at the most reactive site for isolated-pentagon isomers of fullerenes. *Phys. Chem. Chem. Phys.* **2000**, *2*, 3121–3125. [[CrossRef](#)]
30. Lewars, E.G. (Ed.) *The Concept of the Potential Energy Surface*. In *Computational Chemistry: Introduction to the Theory and Applications of Molecular and Quantum Mechanics*; Springer International Publishing: Cham, Germany, 2016; pp. 9–49. [[CrossRef](#)]

31. Machado, D.F.S.; Lopes, T.; Lima, I.T.; Filho, D.A.D.S.; De Oliveira, H.C.B. Strong Solvent Effects on the Nonlinear Optical Properties of Z and E Isomers from Azo-Enaminone Derivatives. *J. Phys. Chem. C* **2016**, *120*, 17660–17669. [[CrossRef](#)]
32. Pegu, D. Solvent effects on nonlinear optical properties of novel para-nitroaniline derivatives: A density functional approach. *Int. J. Sci. Res.* **2014**, *3*, 469–474.
33. Rajkumar, R.; Kamaraj, A.; Bharanidharan, S.; Saleem, H.; Krishnasamy, K. Synthesis, spectral characterization, single crystal X-ray diffraction and DFT studies of 4-((2,4,5-triphenyl-1H-imidazol-1-yl)methyl)pyridine derivatives. *J. Mol. Struct.* **2015**, *1084*, 74–81. [[CrossRef](#)]



© 2020 by the authors. Licensee MDPI, Basel, Switzerland. This article is an open access article distributed under the terms and conditions of the Creative Commons Attribution (CC BY) license (<http://creativecommons.org/licenses/by/4.0/>).